ORIGINAL ARTICLE

Nishant Mistry[ID] · **Leonhard Hitzler** · **Abhishek Biswas** ·
Christian Krempaszky · **Ewald Werner**

Predicting anisotropic behavior of textured PBF-LB materials via microstructural modeling

Abstract It is well established that large temperature gradients cause strong textures in as-built metal parts manufactured via laser beam powder bed fusion. Columnar grains with a preferred crystallographic orientation dominate the microstructure of such materials resulting in a pronounced anisotropic mechanical behavior. Such materials are often studied with the help of tensile tests and corresponding numerical simulations in different loading directions. For the purpose of simulations, the microstructure is usually modeled with a statistically representative volume element (RVE). In the present study, two RVE modeling techniques, based on different texture sampling algorithms, have been compared for their property prediction capabilities. It was found that the model, based on an equally weighted crystallographic orientations set, sufficiently predicted macroscopic mechanical properties and also reduced the computational cost. Furthermore, an efficient method to rotate the boundary conditions for tensile test simulations under different loading directions was developed, thereby reducing the required number of RVE models to just one. The method was compared with an alternate method, where, an RVE model with rotated microstructure was subjected to unchanged boundary conditions. For this study, tensile test simulation results were compared with data from destructive material tests for predominantly single-phase austenitic stainless steel (EN 1.4404/AISI 316L).

Keywords Anisotropy · Rotation of boundary conditions · Stainless steel 316L · Microstructural modeling

N. Mistry (✉)· L. Hitzler · C. Krempaszky · E. Werner
Chair of Materials Science, Technical University of Munich, Boltzmannstraße 15, 85748 Garching, Germany
E-mail: nishant.mistry@tum.de

L. Hitzler
E-mail: leonhard.hitzler@tum.de

C. Krempaszky
E-mail: christian.krempaszky@tum.de

E. Werner
E-mail: ewald.werner@tum.de

A. Biswas
VTT Technical Research Centre of Finland Ltd., Vuorimiehentie 2, 02150 Espoo, Finland
E-mail: abhishek.biswas@vtt.fi

1 Introduction

Conventional manufacturing techniques, such as casting, forging and machining, not only impose inherent restrictions on the geometrical freedom of design, but also lead to material wastage due to their subtractive nature. These limitations can be overcome with the advent of additive manufacturing (AM) methods. In contrast to the subtractive process of removing material from the bulk, AM processes incrementally generate parts by adding material, layer-by-layer, to a build platform [1]. Therefore, AM provides an unprecedented freedom of design, enabling complex, topology optimized geometries to be produced with relative ease. Being compatible with a wide range of materials, including metals, plastics and ceramics, AM is suitable for small- to medium-scale applications in the aerospace, biomedical and automotive industries [1].

The laser beam powder bed fusion (PBF-LB) process is an AM technique capable of producing complex metallic structures [2]. A 3D computer aided design (CAD) model is converted into a sequentially sliced model, containing cross-sections of the model with a predefined thickness equal to the layer thickness. During the PBF-LB process, each of these slices is built with the help of a scanning laser by selectively melting the powder layer on the build platform in a particular pattern, also known as the scan pattern. The energy deposited by the laser beam to the targeted area, while scanning individual vectors, forms a melt pool [2]. This melt pool solidifies rapidly as the heat source, i.e., the laser beam, moves to a new location. A steep temperature gradient of $\sim 10^6$ K/m and a high cooling rate of $\sim 10^6$ K/s have been previously reported to occur during the PBF-LB process involving full melting of metal powder [2,3]. In case the chemical composition and the crystal structure of the newly added layer of metal is identical to that of the substrate, nucleation of new grains may not be required [3]. Rather, epitaxial grain growth takes place in the direction of temperature gradient, i.e., the build direction, resulting in a strongly textured and hierarchical microstructure with elongated grains in the build direction [4,5]. For materials that exhibit anisotropy due to texture, for example stainless steels, Co–Cr alloys, magnesium alloys, etc., the final parts produced by PBF-LB process exhibit significantly different mechanical behavior in comparison with that produced conventionally [6,7].

PBF-LB process parameters, such as laser power, scan pattern, laser beam profile, scan speed, layer thickness, etc., have a direct impact on the resulting microstructure, which, in-turn, influences the macroscopic properties of the produced parts. This unravels the possibility to locally tailor the microstructure such that application-specific functionally graded parts can be produced by varying the PBF-LB parameters during the process [8,9]. The key for achieving this objective in a controlled manner is to comprehend the PBF-LB process parameter–microstructure–property relationship, which has recently received considerable amount of attention [8,9].

In order to predict the mechanical behavior of components with locally varying microstructural properties, numerical simulation is a useful tool. Multi-scale computational models are able to establish the required micro–macro structure–property relationship [10–12]. Provided that the length scales can be separated, a statistically representative microstructural volume element (RVE) can be implemented to study the influence of fluctuating microscopic fields at the macro-level [13,14]. RVE simulations are often coupled with crystal plasticity (CP) models in order to study the effect of grain shapes, sizes, crystallographic orientations, etc., on the mechanical response [15]. A full micro–macro coupling, whereby each macroscopic material point is characterized by the behavior of the microstructure model assigned to it, is required to perform complete component simulations. Such simulations are computationally expensive, thus, the underlying microstructure must be modeled with a minimum amount of details required to accurately predict the sought macroscopic property. The present paper, thus, describes an efficient and fast implementation of RVEs based on a minimum amount of microstructural features needed to predict macroscopic properties like elasticity and plastic yielding of predominantly single phase, additively manufactured metallic materials. Such minimalistic microstructure models may reduce the endured computational cost while optimizing a fully coupled component model.

To study the influence of the PBF-LB process parameters on the microstructure, it is necessary to build and to validate RVE models corresponding to each PBF-LB parameter set. The homogenized mechanical responses of the RVEs can then be compared with corresponding uniaxial tensile tests performed on standard samples produced for each parameter set. However, for materials exhibiting significant anisotropy, the uniaxial tensile loading has to be applied in multiple directions relative to the microstructure in order to characterize the mechanical response [7,16]. From the modeling point of view, this can be achieved either by rotating the applied mechanical boundary conditions relative to the RVE, or by rotating the microstructure within the RVE, thereby allowing the boundary conditions to remain unchanged. Provided that the implementation of these methods is accurate, they must lead to the same stress state in the material. Furthermore, the application of loading in terms of force or displacement boundary conditions to the RVE must ensure a uniaxial stress state
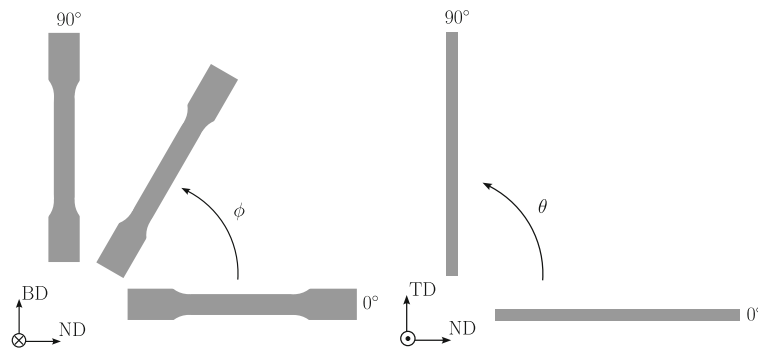
Fig. 1 Schematic diagram of the SS316L sample orientations (adapted from [16])

for each simulation with varying loading directions. Therefore, the current study revisits the implementation of these boundary conditions and provides a comparative study between the strategies to simulate tensile tests in different loading directions. Crystal plasticity enhanced finite element (FE) simulations have been validated against experiments carried out on textured EN 1.4404/ AISI 316L stainless steel (SS316L) samples [7,16].

2 Experimental data

2.1 Mechanical testing

In order to build a virtual 3D RVE model and to validate its mechanical response, microstructural data, as well as the mechanical test results of SS316L samples, have been adopted from previous investigations [7,16]. A few salient features of these investigations are briefly presented here in order to encapsulate the scope of the current study. Near net-shaped samples oriented in different directions were produced via PBF-LB process. Different sample orientations were obtained by varying the polar (θ) and the azimuth (ϕ) angles (Fig. 1). Five configurations ($\phi = 0°$, $15°$, $45°$, $75°$ and $90°$) were produced for the polar angle $\theta = 0°$, i.e., in the plane spanned by the build direction (BD) and the normal direction (ND). An additional configuration was produced along the transverse direction (TD) (i.e., $\theta = 90°$ and $\phi = 0°$). A brief summary of the utilized process parameters and the chemical composition of the samples can be found in "Appendix B". Prior to testing, these samples were machined to their final dimensions in accordance with DIN 50125–Type E $5 \times 10 \times 40$. Destructive tensile tests were performed on these samples to determine the elastic and plastic properties of the material.

The bulk material properties of these samples were found to be homogeneous based on two findings. Firstly, the macro-hardness of the machined samples was consistent and did not exhibit a location-dependent scatter. Secondly, fracture occurred arbitrarily along the gauge length during tensile tests. Relative density investigations via Archimedes principle revealed that all samples had a relative density greater than 99% (machined conditions), thus, they were considered 'fully dense' as per the standardized quality requirements [17].

2.2 Microstructural analysis

In as-built condition at room temperature, additively manufactured SS316L samples predominantly consist of austenitic grains with a face-centered cubic (FCC) lattice [18]. To reveal the crystallographic orientation as well as the morphology of these grains, electron backscatter diffraction (EBSD) measurements were previously performed on the set of samples described in Sect. 2.1. Figure 2 presents the unpublished results of these measurements carried out for three samples with different orientations. The raw data obtained from EBSD measurements was analyzed using the MTEX toolbox [19].

Most grains had an elongated columnar-like shape with the axis of elongation in the BD (Fig. 2). The average grain diameter, evaluated from the grain size distribution of these samples, was approximately $19 \, \mu m$, with a large standard deviation of $17 \, \mu m$. Also, elongated grains larger than $100 \, \mu m$ were observed, whereas the layer thickness utilized during the process was $30 \, \mu m$ [16]. Furthermore, the melt pool boundaries, reported by Hitzler et al. [16] in the cross-sectional micrographs of these samples, are not observed in Fig. 2, indicating
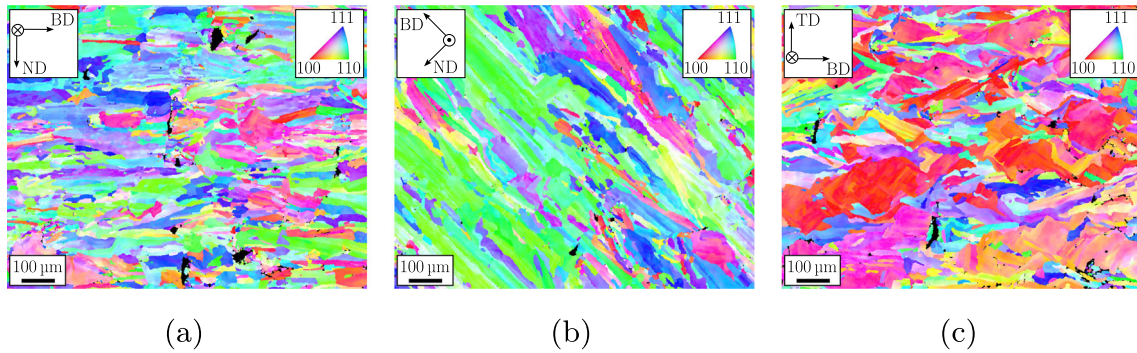
Fig. 2 EBSD inverse pole figure map representing the texture present in the SS316L samples with orientations **a** $\phi = 0°$, $\theta = 0°$ (TD-axis pointing into the plane) **b** $\phi = 45°$, $\theta = 0°$ (TD-axis pointing out of the plane) and **c** $\phi = 0°$, $\theta = 90°$ (ND-axis pointing into the plane)
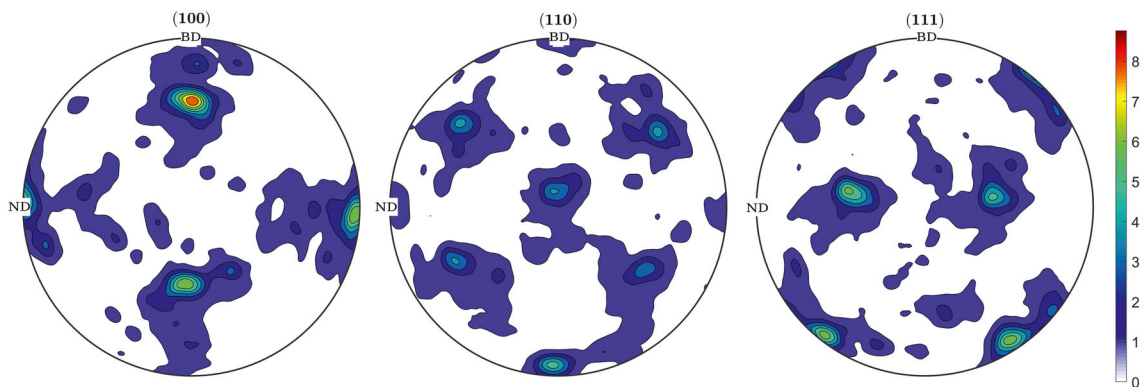
Fig. 3 Equal area pole figure obtained from EBSD experiments

an epitaxial grain growth across deposited layers. The clustered non-indexed points, represented in black in Fig. 2, are due to the defects present in the samples, which could also be observed in the micrographs.

Appropriate rotations were applied to these EBSD measurements, and all measured grain orientations were obtained on the BD–ND plane. Figure 3 represents the pole figure based on the complete set of EBSD measurements (i.e., approximately 4000 grain orientations). A strong $\langle 110 \rangle$ texture along the BD can be observed in the pole figure. This is in agreement with the observations reported in other investigations on SS316L microstructures obtained via PBF-LB [20,21]. On a side note, a strong $\langle 100 \rangle$ texture along BD has also been frequently reported for SS316L microstructures [3]; however, resulting texture in the material is strongly influenced by the scanning strategy and the laser power [22,23]. For example, Casati et al. [24] managed to avoid the formation of a strong texture by rotating the scanning direction by 67° after each layer. Marattukalam et al. [22] succeeded in tailoring crystallographic textures locally within a single component by switching scanning strategies while building individual layers. A change in the scanning strategy in successive layers may disrupt the epitaxial grain growth, which, in-turn, may reduce the induced anisotropy [24]. A thorough understanding of the underlying principle of texture formation during PBF-LB and its linkage to the process parameters is currently not well established.

3 Constitutive model

For this study, a virtual microstructure model was developed with the commercially available numerical solver package ABAQUS [25]. The periodicity of these microstructure models were achieved following the model development process presented by Fischer et al. [26] using microstructural model development software packages Voro++ [27] and Neper [28]. In order to take into account the deformation behavior of individual grains and to capture the influence of microstructural features, such as texture, on the macroscopic properties

of the material, the micromechanics–based crystal plasticity simulation kit, DAMASK [29], was incorporated via a user subroutine into the numerical model.

In crystalline materials, such as the austenitic SS316L, plastic deformation occurs predominantly due to slip, i.e., dislocation glide in close packed crystallographic planes [30]. A slip plane along with the direction of slip constitute a slip system. In FCC crystals, slip is observed almost exclusively on the twelve $\{111\}\langle\bar{1}10\rangle$ slip systems. A slip system becomes activated once the critical value of shear stress is exceeded on that particular system. Hence, the anisotropy of a polycrystalline aggregate, caused by texture on a macroscopic level, can be captured by incorporating the crystallographic orientations of the grains into the numerical model at the microscopic level [31,32]. This was implemented using a phenomenological crystal plasticity model. Although phenomenological crystal plasticity models cannot capture path- and size-dependence due to the fact that they do not consider lattice defect populations [15], they provide the best possible compromise between accuracy and computational effort [31].

3.1 Kinematics

In a continuum mechanical framework, the total deformation gradient $\mathbf{F}$ describes the deformation of a material point of the macrostructure. The total deformation gradient can be multiplicatively decomposed as follows:

$$\mathbf{F} = \mathbf{F}_e \cdot \mathbf{F}_p, \tag{1}$$

where $\mathbf{F}_e$ and $\mathbf{F}_p$ describe the elastic and the plastic parts of the deformation gradient, respectively. As discussed earlier, slip in an FCC crystal occurs in twelve slip systems; thus, the plastic velocity gradient $\mathbf{L}_p$ can be determined by the sum of slip rates $\dot{\gamma}$ on all active slip systems:

$$\mathbf{L}_p = \dot{\mathbf{F}}_p \, \mathbf{F}_p^{-1} = \sum_{i=1}^{N_{\text{slip}}=12} \dot{\gamma}^i \, \mathbf{m}^i \otimes \mathbf{n}^i, \tag{2}$$

where $\mathbf{m}^i$ and $\mathbf{n}^i$ denote the slip direction and the slip plane normal for the ith system, respectively.

3.2 Phenomenological constitutive relations

The second Piola–Kirchhoff stress measure $\mathbf{S}_e$ represents the response of the crystal to the applied elastic Green–Lagrange strain $\mathbf{E}_e$, thus, forming a conjugate pair related by:

$$\mathbf{S}_e = \mathbb{C} : \mathbf{E}_e = \mathbb{C} : \frac{1}{2} \left(\mathbf{F}_e^T \, \mathbf{F}_e - \mathbf{I} \right), \tag{3}$$

where $\mathbb{C}$ is the fourth-order tensor representing the elastic stiffness of the material and $\mathbf{I}$ is the identity tensor. For a cubic crystal lattice, such as the austenitic SS316L, $\mathbb{C}$ is determined by three constants (C_{11}, C_{12} and C_{44}) due to its symmetry properties [33]. For simulations in the current work, elastic constants, based on the experiments performed by Ledbetter et al. [34] on single crystals of a similar stainless steel grade (AISI 304), were adopted. Table 1 lists these elastic constants along with other constitutive model parameters.

The shear rate on a system is governed by the resolved shear stress on the system. The resolved shear stress τ on the ith slip system is determined by Schmid's shear stress law as follows:

$$\tau^i = \mathbf{F}_e^T \, \mathbf{F}_e \, \mathbf{S} : \left(\mathbf{m}^i \otimes \mathbf{n}^i \right). \tag{4}$$

Furthermore, the relation between resolved shear stress and shear rate on a system is given by the phenomenological power law [35]:

$$\dot{\gamma}^i = \dot{\gamma}_0 \left| \frac{\tau^i}{\tau_c^i} \right|^n \text{sgn} \left(\tau^i \right), \tag{5}$$

where $\dot{\gamma}_0$ is the initial shear rate and τ_c^i is the initial critical resolved shear stress assumed to be equal on all slip systems. A weak rate dependence was assumed for the simulations by selecting a strain rate-dependent

Table 1 Phenomenological crystal plasticity constitutive model parameters for SS316L

Elasticity		Plasticity	
C_{11}	204.6 GPa*	τ_0	208 MPa
C_{12}	137.7 GPa*	τ_∞	327 MPa
C_{44}	126.2 GPa*	h_0	1000 MPa
		$\dot{\gamma}_0$	$0.001\,\text{s}^{-1}$
		n	20
		a	1.75

*Elastic constants obtained from AISI 304 single crystal experiments [34]

exponent n value of 20 in Eq. 5 [31,36]. The critical resolved shear stress evolves according to the following relation:

$$\dot{\tau}_{\text{c}}^i = \sum_{n=1}^{12} h_{ij}\,|\dot{\gamma}^j|, \tag{6}$$

where h_{ij} represents the hardening matrix which accounts for the interactions among different slip systems and is given by:

$$h_{ij} = q_{ij}\left[h_0\left(1 - \frac{\tau_{\text{c}}^i}{\tau_\infty}\right)^a\right]. \tag{7}$$

In Eq. 7, h_0, a and τ_∞ represent the self-hardening coefficient, the hardening exponent and the saturation value of slip resistance, respectively. These values were assumed to be equal for all FCC slip systems. The parameter q_{ij} accounts for the latent hardening. As per the common practice, a value of 1.0 was assumed for the case of coplanar slip systems (i.e., $i = j$) and 1.4 for the case of non-coplanar slip systems (i.e., $i \neq j$), which rendered the hardening model anisotropic [15]. Numerical predictions for deformation texture development, based on these values, agree well with the experiments for FCC polycrystals [37]. The remaining parameters in Table 1 provided a best fit to the experimental data, taken as a reference for this study.

4 Boundary conditions

In agreement with the classical homogenization approach, geometric periodicity of the microstructure was assumed. From the modeling point of view, this was achieved by prescribing periodic boundary conditions to the RVE following Li and Sitnikova [38], such that, it mimicked an infinitely extended microstructure. The net displacement between two congruent points on the opposite faces of an RVE was then tied to a 'master node'. Hence, for a 3D RVE, a set of three master nodes, in x, y and z directions, was sufficient to apply mechanical loads in the form of force or displacement boundary conditions at these master nodes. For the present work, mechanical loads were applied in the form of displacement boundary conditions at the master nodes. The heterogeneities present in the material, i.e., grain boundaries and other defects, were assumed to be small enough such that the material could be considered homogeneous on the macroscale [14]. This assumption was justified since the samples were reported to be homogeneous [16]. Hence, the volume averaged stress response of the RVE, due to the applied displacements at the master nodes, could be considered representative of the material behavior [13].

For the purpose of presenting the boundary conditions and subsequent rotations, the BD, ND and TD axes were considered to be the x, y and z axes in the following Subsections, respectively.

4.1 Uniaxial tension boundary condition

In principle, the macroscopic deformation gradient tensor $\mathbf{F}_{\text{M}}$ formulates the displacement boundary conditions needed to be imposed on the RVE [38]. Henceforth, the subscript 'M' denotes macroscopic quantities. In other words, the columns of the component matrix of $\mathbf{F}_{\text{M}}$ represent the displacements needed to be assigned to the master nodes. However, to ensure a unique solution, rigid body translation and rotation of the model must be

eliminated. Rigid body translation of the RVE can be restricted by constraining the translational motion of a corner node. To restrict rigid body rotation of the RVE, the macroscopic deformation gradient tensor $\mathbf{F}_M$ has to be considered. Polar decomposition of deformation gradient reveals the orthogonal rotation tensor $\mathbf{R}_M$ and the symmetric stretch tensor $\mathbf{v}_M$ as follows:

$$\mathbf{F}_M = \mathbf{v}_M \, \mathbf{R}_M. \tag{8}$$

If no macroscopic rigid body rotation of the RVE occurs, $\mathbf{R}_M$ can be set equal to the identity tensor $\mathbf{I}$, which renders:

$$\mathbf{F}_M = \mathbf{v}_M. \tag{9}$$

Since the stretch tensor $\mathbf{v}_M$ is symmetric, Eq. 9 renders $\mathbf{F}_M$ to be symmetric by further introducing additional kinematic constrains between the non-diagonal components of $\mathbf{F}_M$ as follows:

$$F_{12} = F_{21}, \quad F_{23} = F_{32} \quad \text{and} \quad F_{13} = F_{31} \tag{10}$$

or

$$\mathbf{F}_M = \begin{bmatrix} a & d & e \\ & b & f \\ \text{sym.} & & c \end{bmatrix}. \tag{11}$$

If the applied boundary conditions adhere to Eq. 10 throughout the simulation, macroscopic rigid body rotation of the model is avoided. These constrains were incorporated into the simulations presented in this study. It is to be noted that often rotation is constrained by setting the non-diagonal terms equal to zero with the tacit assumption that the principal directions of stress and strain tensors align with the loading direction. However, for anisotropic behavior of the RVE, which may be the behavior of a polycrystalline aggregate manufactured additively, this may not be the case and thus, the non-diagonal terms were not predefined in the current study.

For the case of uniaxial loading, for example, a 5% engineering strain applied in the BD (x-direction), only the component a in Eq. 11 must be assigned a value, thus,

$$\mathbf{F}_M = \begin{bmatrix} 1.05 & * & * \\ & * & * \\ \text{sym.} & & * \end{bmatrix}. \tag{12}$$

The components $b - f$ need not be provided a priory, thus, ensuring a uniaxial stress state irrespective of the constitutive behavior. These values are obtained depending upon the microstructural response to the applied mechanical load.

4.2 Tensile test simulations in different loading directions

The microstructures of the samples oriented in different directions may vary owing to several factors such as the direction of heat flow, number of deposited layers, etc. However, from the modeling point of view, a statistically representative microstructure model, which can reproduce the experimental results for all samples, is desired. This model is required to be mechanically loaded in different directions, which can be achieved with two possible and alternate methods as described in the following Subsections.

4.2.1 Method I: rotation of the boundary conditions

A 2D implementation of the rotated boundary conditions can be found in literature [36,39]. However, these implementations require that all components of the deformation gradient $\mathbf{F}_M$ are known a priori. A 3D implementation similar to Fillafer et al. [40] is presented here, which needs no such information. The advantage of this method is that the RVE has to be created only once. Assuming a rotation about the TD axis (z-axis) by an angle ϕ, considering Eq. 11, the rotated deformation gradient takes the form:

$$\begin{aligned} \tilde{\mathbf{F}}_M &= \mathbf{R}_z^T \, \mathbf{F}_M \, \mathbf{R}_z \\ &= \begin{bmatrix} aC^2 + bS^2 + 2dCS & CS(b-a) + d(C^2 - S^2) & Ce + Sf \\ & aS^2 + bC^2 - 2dCS & Cf - Se \\ \text{sym.} & & c \end{bmatrix}, \end{aligned} \tag{13}$$
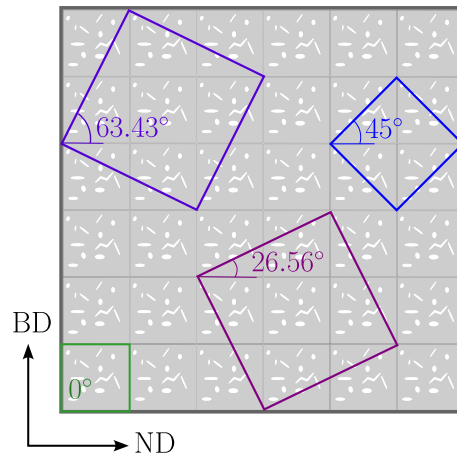
Fig. 4 Schematic representation of large volume elements cut out from a periodic microstructure. Note, each large volume element is itself periodic

(a)   (b)
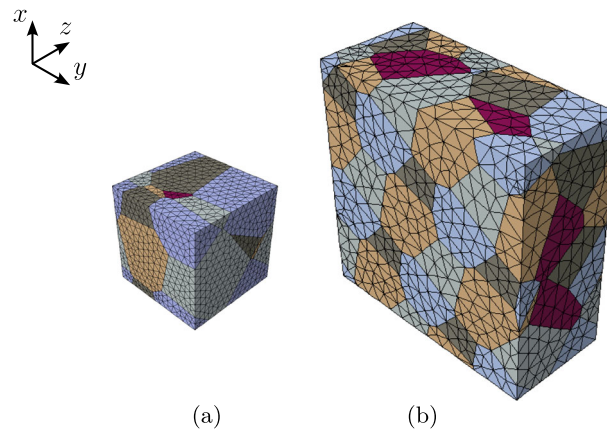
Fig. 5 RVE models with boundary conditions according to **a** method I and **b** method II

where $C = \cos(\phi)$ and $S = \sin(\phi)$. In the present work, only a rotation about the TD axis (z-axis) was considered; however, an arbitrary combination of rotations can be applied.

Since $\tilde{\mathbf{F}}_M$ denotes the rotated deformation gradient, displacements to the RVE boundaries have been assigned via a set of three intermediate dummy nodes. The dummy node displacements, representing the components of $\tilde{\mathbf{F}}_M$, were coupled to the displacements of the three master nodes, representing the components of $\mathbf{F}_M$, according to Eq. 13. For uniaxial tensile loading in different directions, only the angle ϕ had to be varied in Eq. 13.

4.2.2 Method II: rotation of the microstructure

Another approach is to rotate the underlying microstructure (i.e., the grains along with their crystallographic orientations) within the RVE, while keeping the boundary conditions unchanged [41]. However, geometric periodicity of the microstructure must be ensured in the process. To preserve geometric periodicity, reasonably large volume elements inclined at various angles were cut from the microstructure. Considering an arbitrary RVE of unit size, which is geometrically periodic in the BD, the ND and the TD directions, a microstructure can be constructed by stacking this RVE in the BD–ND plane as shown in Fig. 4. Large periodic volume elements can then be cut from this microstructure for various angles as shown. In the BD–ND plane, they appear as squares with their corners coinciding with the grid formed by the underlying RVEs.

These large volume elements with rotated microstructure exhibit redundant translational symmetries in the sense that repeated grain structures can be found in them. Although this shall not affect the volume averaged stress response of these large volume elements, the presence of translational symmetries will result in exactly
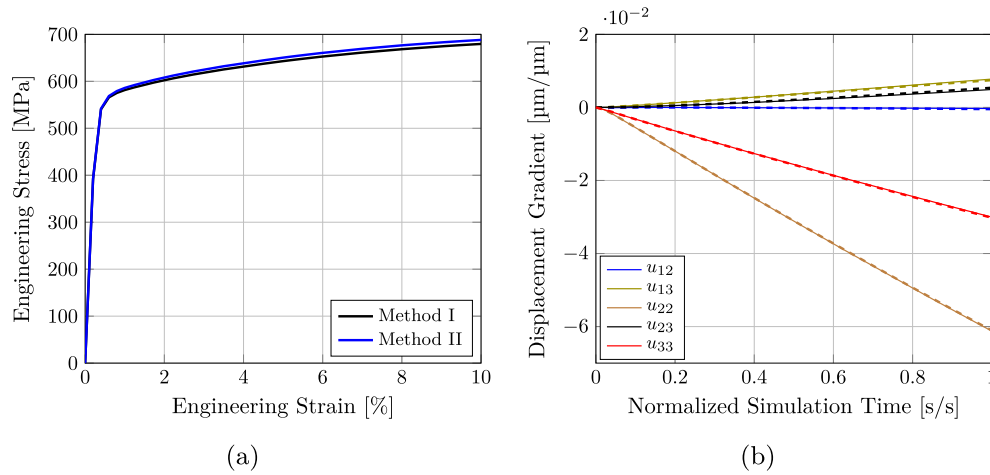
Fig. 6 A comparison between methods I and II **a** engineering stress versus strain **b** components of displacement gradient tensor for method I (solid lines) and method II (dashed lines)

the same outcome in terms of stress distribution at an expense of additional computational resource [38]. The computational cost is directly proportional to the volume of the model and thereby, depends on the angle of inclination as described in "Appendix A". Indeed, a periodic RVE with five grains was created and an engineering strain of 10% was applied at an inclination of 26.56° to the x-axis as per method I. Further, a large volume element with the microstructure rotated by 26.56° about the z-axis was generated with method II and an engineering strain of 10% was applied in the x-direction as shown in Fig. 5. Each grain was made up of approximately 400 second-order tetrahedral continuum elements [25] as they have been known to model grain boundaries efficiently [31]. The grains were assigned arbitrary crystallographic orientations along with the material model, as described in Sect. 3. This was to ensure that the response of the RVE to the applied boundary conditions was the same, irrespective of the constitutive behavior of the polycrystal. Figure 6a shows the engineering stress–strain response of the RVEs. The difference between the engineering stress response of the RVEs was less than 1% at an engineering strain of 10%; hence, they delivered almost identical predictions. This small discrepancy could be attributed to the changes in the mesh of the grains at the RVE boundaries due to different cutting planes encountered by the grains.

Furthermore, Fig. 6b provides a comparison of all other components of the deformation gradient $\mathbf{F}_M$ during the simulation in terms of displacement gradient $\mathbf{u}_M$ (since, $\mathbf{u}_M = \mathbf{F}_M - \mathbf{I}$). It was observed that all displacement gradient components in both models remained the same throughout the simulation, which ensured the uniqueness of the solution satisfying the constraining Eq. 13. Taking into consideration the calculation and model build-up times, method I required considerably less effort. Therefore, method I was implemented for all further simulations presented in this study, by applying rotations to the boundary conditions.

5 Simulation model development

The crystallographic texture is generally mathematically described using a continuous function f, which is referred to as the orientation distribution function (ODF). This function can be represented through kernel density estimations on the rotation group $SO(3)$ [42], using a non-negative kernel (ψ) with finite Fourier series expansion [43].

The ODF (f) is estimated from the crystallographic measurements g_i, $i = 1, \ldots, N$ from experiments like EBSD by

$$f(g) = \frac{1}{N} \sum_{i=1}^{N} \psi_\kappa(\omega(g_i, g)), \quad g \in SO(3), \tag{14}$$

where $\omega(g_i, g)$ is the disorientation between g_i and g. N is the total number of orientation measurements. Usually, EBSD experiments provide a large number of crystallographic orientations and for the sake of computational feasibility, a smaller number $(\hat{N})$ of discrete orientations $\hat{g}$ are required. Therefore, the ODF estimated

from the EBSD measurements was suitably reconstructed using a smaller number of discrete orientations. In this work, two different RVEs were used for property prediction based on different texture reconstruction algorithms, which were implemented in MTEX [19].

5.1 Weighted texture reconstruction

A set of weighted orientations was sampled using a density-based clustering algorithm of the crystallographic orientations, as suggested by Wang et al. [44], where the weight of an orientation represented the normalized volume of the corresponding grain in the RVE. Each grain had an orientation $\hat{g}_i$ with weight w_i, $i = 1, \ldots, \hat{N}$, where $\hat{N}$ represents the number of grains. The ODF from the sampled orientations was estimated as

$$\hat{f}(g) = \sum_{i=1}^{\hat{N}} w_i \psi_\kappa(\omega(\hat{g}_i, g)). \tag{15}$$

The L_1 ($= ||f - \hat{f}||_1$)-error between f and $\hat{f}$ was used to judge the ability of the sampled orientations to closely approximate the experimentally measured orientations in EBSD.

A set of 400 weighted orientations was found to capture the experimental ODF within a 10% error (Fig. 7). With a grain size distribution (Fig. 8a) in accordance with the obtained weight distribution, an RVE model with 400 equiaxed grains (Fig. 8b) was built such that the average grain size matched the experimentally determined value of 19 μm. In order to efficiently resolve the grain boundaries, each grain was meshed with approximately 400 second- order tetrahedral continuum elements [25]. The choice of equiaxed grains was based on the numerical investigations by Fischer et al. [31] and Biswas et al. [32] studying the influence of grain shape on macroscopic property predictions. Both studies concluded that grain shape, as compared to crystallographic texture, had little influence on the stress–strain response of the RVE. Hence, columnar grains, which usually require large number of small elements to mesh its sharp edges, were avoided. Rather, emphasis was laid upon texture reconstruction.

5.2 Equally weighted texture reconstruction

Another approach is to sample a large number of equally weighted orientations. For such sampling, the texture reconstruction algorithm suggested by Biswas et al. [45] was employed. A set of 729 equally weighted orientations was found to effectively reconstruct the texture within a 10% error (Fig. 9). The ODF and L_1-error of the equally weighted orientations were estimated using the aforementioned equations. Correspondingly, the RVE consisted of 729 cube shaped grains with equal volumes (Fig. 10) such that the diameter of an equivalent sphere of corresponding volume would amount to 19 μm. Each grain was meshed with 8 linear hexahedron continuum elements.
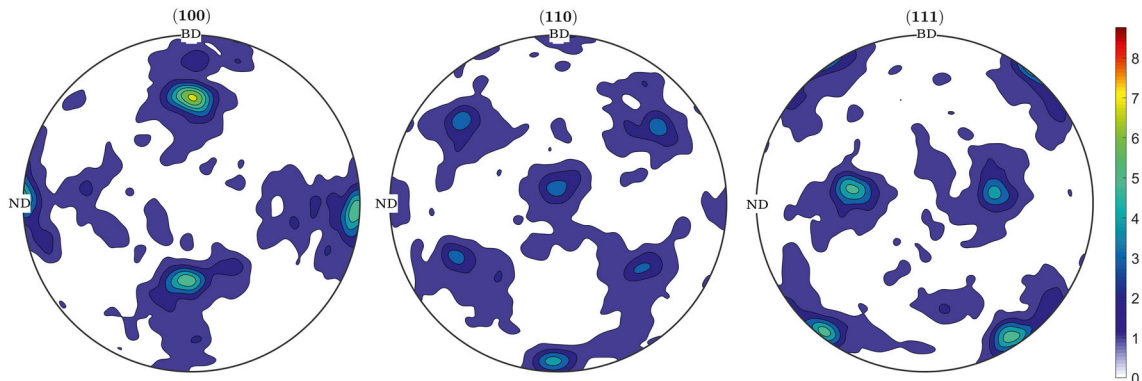
Fig. 7 Pole figure based on the reduced set of weighted orientations following Wang et al. [44]

(a) Grain size distribution (b) RVE with 400 grains
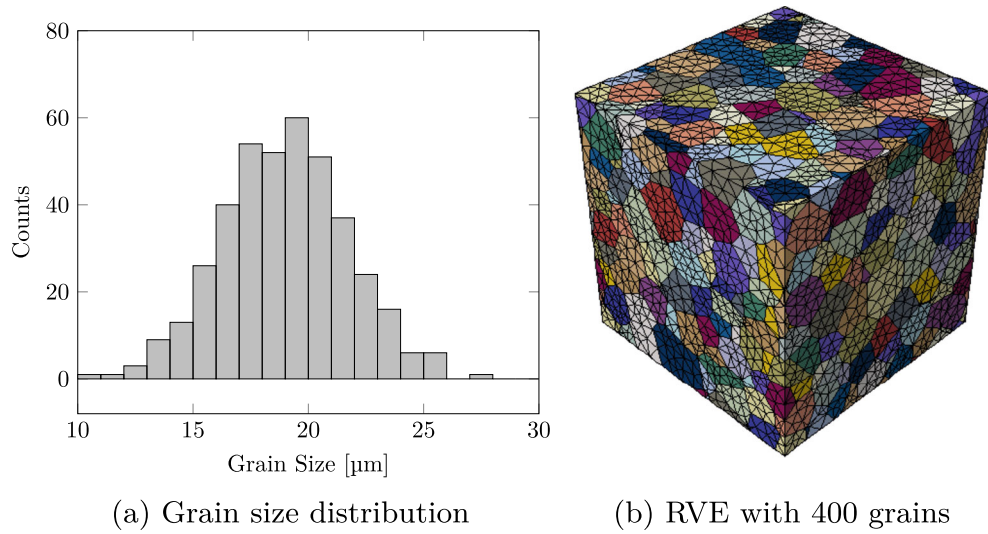
Fig. 8 RVE model with equiaxed grains of varying sizes according to the weight distribution of orientations
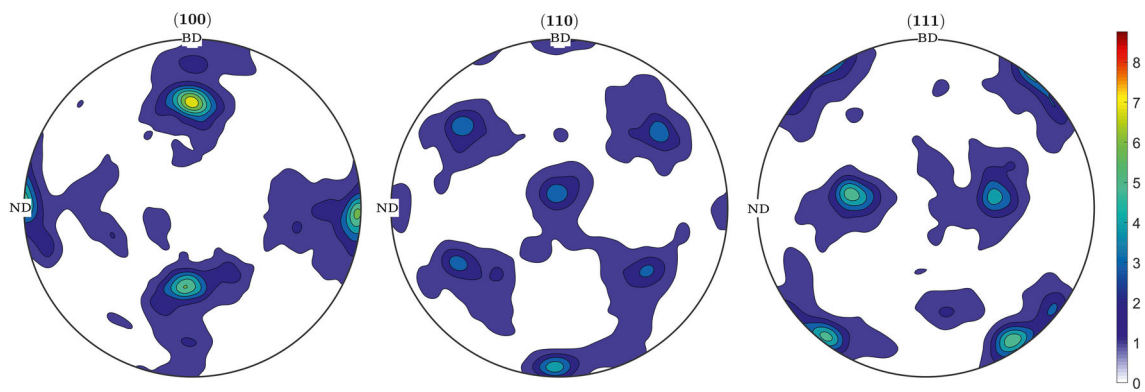
Fig. 9 Pole figure based on the reduced set of equally weighted orientations following Biswas et al. [45]
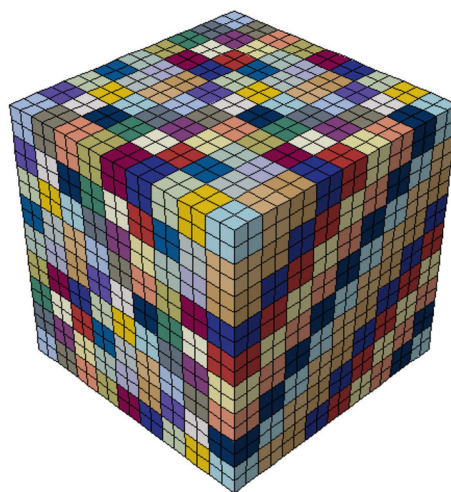
Fig. 10 RVE model with 729 equal volume grains based on the equally weighted orientations

6 Results and discussions

6.1 Model selection

Both texture reconstruction algorithms closely captured the experimental ODF; however, the RVEs based on these algorithms consisted of different sizes, shapes and numbers of grains. In order to compare their property prediction capabilities, a 5% engineering strain was applied in the x-direction to both models. From the simulation results presented in Fig. 12, it can be observed that both models provided comparable predictions for the macroscopic stress–strain response. The comparison insinuated the significance of capturing the orientation distribution over other microstructural features. This was in agreement with the findings of Fischer et al. [31] and Biswas et al. [32] on the little influence of grain shape and misorientation distribution, respectively. Moreover, the grain size distribution also exhibited little influence on the macroscopic response. This was due to the inability of the material model to incorporate the size dependence, as discussed previously in Sect. 3. Strain gradient-based plasticity models, which are computationally expensive, are able to capture this effect [15] and will be incorporated in future studies.

Although the volume averaged quantities were in a good agreement, the stress distribution within the RVEs (Fig. 11) varied considerably. In the RVE model with cube-shaped grains with equal volumes (Fig. 11b), stresses appear to be concentrated around the corners of the cube-shaped grains. Such stress concentrations may be unrealistic, hence, a simplified modeling strategy, such as described in Sect. 5.2, may be appropriate

(a) 400 grains with a volume distribution   (b) 729 grains with equal volumes
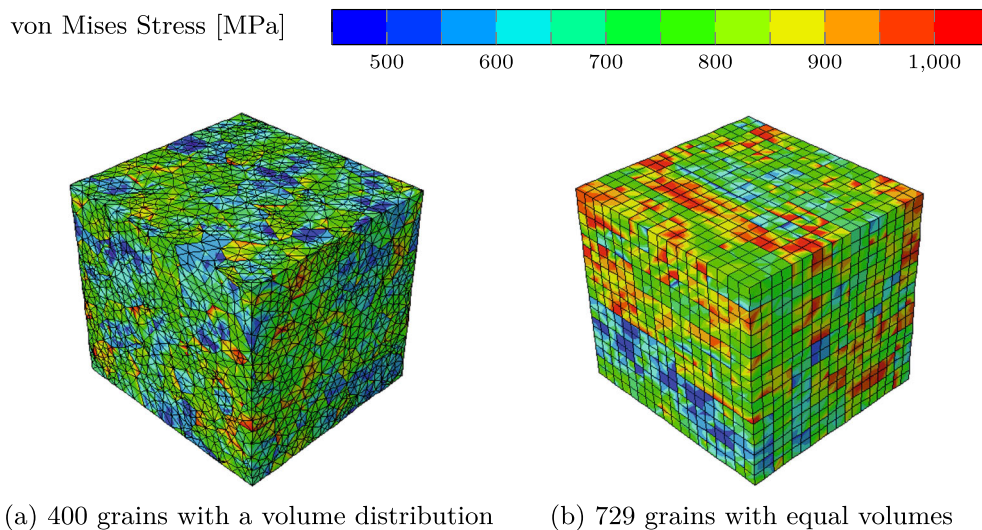
Fig. 11 Stress distribution in RVE models
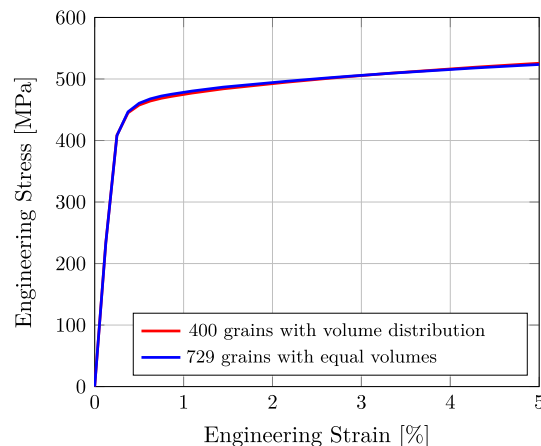
Fig. 12 A comparison between engineering stress versus strain response of both RVE models

only if the scope of the numerical investigation is limited to predicting volume averaged macroscopic material properties. For studies which are strongly influenced by the stress state around the material defects, such as crack initiation and propagation, details such as the grain shape, size and misorientation distribution must be taken into account.

However, the high computational cost required for a detailed model, such as described in Sect. 5.1, may not result in tangible improvements of the volume averaged macroscopic property predictions, as shown in Fig. 12. Thus, the simulations presented, henceforth, were performed with the RVE model made up of cube-shaped grains with equal volumes.

6.2 Tensile test simulations

Tensile test simulations were performed with the RVE made up of cube-shaped grains in different loading directions corresponding to the sample orientations as described in Fig. 1. In addition, two intermediate sample configurations (i.e., $\phi = 30°$ and $60°$, $\theta = 0°$) were simulated; however, experimental investigations were not available for these configurations. A comparison of the simulation results with their corresponding experiments is presented in Fig. 13. The trajectory of the simulated curves qualitatively conformed well with the experiments. Equally weighted grains model was able to closely predict the experimentally observed strength increase from $\phi = 0°$ to $\phi = 45°$ on the BD–ND plane ($\theta = 0°$). The predictions of both Young's modulus and yield strength for the sample orientated along the TD-axis on the ND–TD plane (i.e., $\phi = 0°$ and $\theta = 90°$) were within 5% of the experimentally observed value. Furthermore, the model predicted a decrease in both the Young's modulus and the yield strength for angles greater than $\phi = 45°$; however, it significantly over-predicted these values for both cases, $\phi = 75°$ and $\phi = 90°$. There could be several reasons for the over-prediction of these properties for large polar angles, which are discussed in the following subsections.

6.2.1 Elastic constants

One of the possible reasons for this over-prediction may be related to the elastic constants of the FCC lattice. The present work adopted C_{11}, C_{12} and C_{44} values from experiments performed on AISI 304 single crystal [34] which may deviate from the actual values. Elastic constants based on such experiments for SS316L single crystal may improve the predictive capability of the model.

6.2.2 Heterogeneous microstructure

With increasing projected height of the sample in the BD, the number of deposited layers and thereby, the runtime of the process increases. It suggests that for these samples, the layers at the bottom section of the sample would have undergone a larger number of reheating cycles. Such a reheating pattern may alter the
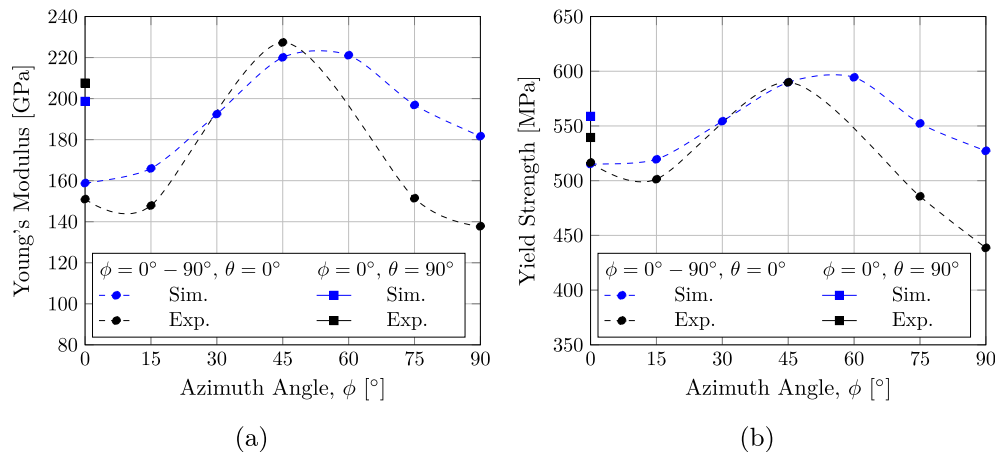
Fig. 13 A comparison between simulation results and experiments for different sample orientations **a** variation of Young's modulus **b** variation of yield strength

microstructure, especially the dislocation density, at the bottom layers creating a gradation of microstructural features along the BD. This may add to the exhibited anisotropic yielding behavior [46]. The gradation effect should have been evident through the variation of hardness test results carried at several locations along the sample length and also through a predominant rupture on either the upper or the lower end of the sample during tensile testing. However, neither was the case [16]. This suggests that additional analyses may be required to deduce a microstructural gradient present in the sample. The microstructure should be studied at various locations, encompassing the height and the runtime dependencies, with the help of EBSD measurements to capture a possible gradient.

6.2.3 Porosity

Porosity has a detrimental effect on the strength of additively manufactured parts [46]. Keyhole pores are known to occur mostly within the solidified melt pool of individual scans, whereas lack-of-fusion pores occur mostly at the tri-junction of two neighboring scans and the layer beneath. Between two successive layers (for example, nth and $(n + 1)$th layer), these lack-of-fusion defects appear to be elongated along the laser scan direction utilized for the $(n + 1)$th layer [46]. This indicates that in-build-plane (ND–TD) orientations of these defects may depend on the scan strategy implemented and their shapes may depend on the hatch distance between laser scans. Due to their elongated shape and preferred orientation, lack-of-fusion defects cause an asymmetrical reduction in the cross-section. The reduction in cross-sectional area is the highest for the out-of-plane direction (BD). These facts may contribute to the anisotropic behavior of the material. However, according to the numerical studies performed by Prasad et al. [47], the effect of asymmetrical area reduction relative to the loading direction leads to significant anisotropic yielding for pore volume fractions exceeding 2%. This finding is in agreement with the experimental observations by Ronneberg et al. [46]. For the investigated samples with residual porosity less than 1%, this implies that the contribution of porosity to the observed anisotropic yielding behavior is negligible. Thus, it is unlikely that incorporating pores into the numerical model would lead to a meaningful improvement of the predictions.

6.2.4 Residual stresses

It is known that in-build-plane residual stresses are usually larger than those in the build direction [48]. Furthermore, only the top and the bottom portions of an additively manufactured part are under tensile residual stresses, whereas the bulk is under compressive residual stresses [49]. This means that the tensile test samples lying horizontally on the build plane have larger compressive residual stresses in the loading direction than the vertical samples. Apart from texture, this may be one of the factors contributing to the observed anisotropy. The current study does not account for these effects which may lead to an over-prediction of the numerical model.

7 Conclusions

In this work, anisotropic behavior of the predominantly single phase additively manufactured austenitic stainless steel 316L was studied with the help of tensile test simulations in different loading directions. The method proposed to rotate RVE boundary conditions was compared with the simulation results of a mechanically equivalent RVE model with rotated microstructure. It was found that the method to rotate boundary conditions was cost effective, considering model build-up and computational efforts, and ensured uniqueness of the solution. Furthermore, on account of the comparative study of the RVE models based on two texture reduction algorithms, it was found that a texture reduction carried out with equally weighted orientation set led to an easy-to-implement RVE model which significantly reduced the computational cost and provided comparable property prediction capability. However, equal volume grains, which were modeled as cubes, were not able to obtain stress distributions within the RVE with a high resolution, thereby, limited the use of such models to the volume averaged macroscopic mechanical properties. The model could capture the observed increase in strength from 0° to 45° in the BD–ND plane; however, the model largely over-predicted the strength in loading directions greater than 45°. Possible reasons for this deviation have been discussed, but further investigations are required before final conclusions on this aspect could be drawn.

Declarations

Conflict of interest The authors have no relevant financial or non-financial interests to disclose.

Appendix A: Calculation of volume increase

An RVE forms the smallest possible, periodically repeating entity of a virtual microstructure. In other words, the microstructure can be synthesized by constructing an infinite grid of this RVE. The same microstructure, however, can be synthesized by an alternate grid, which is inclined at an angle relative to the initial grid, subjected to the constraint that the periodicity of its basic repeating entity is not compromised. To satisfy this constraint, the grid points of the rotated grid must coincide with that of the initial grid. This can only be achieved if the dimensions of the basic repeating entity of the rotated grid are increased. These enlarged entities were denoted as large volume elements.

In principle, a large volume element, inclined at any angle, can be extracted from the microstructure. However, taking the computational cost into consideration, a sensible size of these volume elements can be attained only for a few inclination angles. For example, Fig. 14 depicts a few inclination angles for which the corresponding increase in the volume is less than a thousand times the volume of the initial cubic RVE.
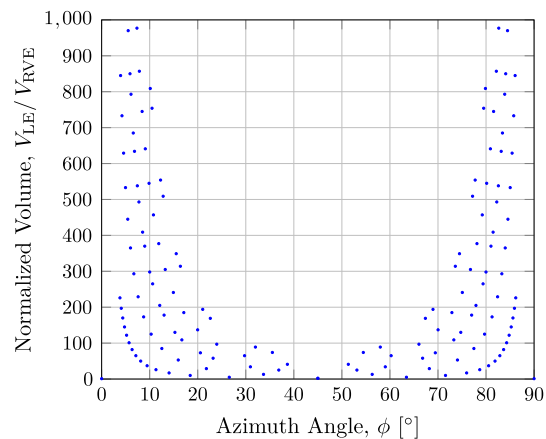
Fig. 14 Volume of large volume elements (V_{LE}) corresponding to their inclination angles normalized with respect to the volume of initial cubic RVE (V_{RVE})

Appendix B: Process parameter set and chemical composition

An SLM 280HL machine (SLM Solutions GmbH, Lübeck, Germany) was utilized to manufacture the samples with process parameters presented in Table 2. A layer thickness of $30\,\mu m$, mounting plate temperature of $200°C$, nitrogen as the inert gas, and a scan vector length of $10\,mm$ were employed to manufacture the samples. Further

Table 2 PBF-LB irradiation parameter set for processing of the SS316L samples [16]

Parameter set	Scan speed (mms^{-1})	Laser power (W)	Hatch dist. (mm)	Rotation angle inc. (°)	Energy density (Jmm^{-3})
Core	800	200	0.12	33	69.4

Table 3 Chemical composition according to DIN EN 10088-3 of the AISI 316L/1.4404 samples as reported by Hitzler et al. [16], in wt.%

Element	Fe	C	Mn	Cr	Ni	Mo	Si	N	P	S
	Bal.	< 0.03	< 2	16.5–18.5	10–13	2–2.5	< 1	< 0.1	< 0.045	< 0.03

details of the manufacturing process can be found in Hitzler et al. [16]. Chemical composition analysis of the manufactured AISI 316L/1.4404 samples is presented in Table 3.

References

1. Gibson, I., Rosen, D.W., Stucker, B.: Additive Manufacturing Technologies. Springer, New York (2015). https://doi.org/10.1007/978-1-4939-2113-3
2. Hitzler, L., Merkel, M., Hall, W., Öchsner, A.: A review of metal fabricated with laser- and powder-bed based additive manufacturing techniques: process, nomenclature, materials, achievable properties, and its utilization in the medical sector. Adv. Eng. Mater. **20**, 1700658 (2018). https://doi.org/10.1002/adem.201700658
3. DebRoy, T., Wei, H.L., Zuback, J.S., Mukherjee, T., Elmer, J.W., Milewski, J.O., Beese, A.M., Wilson-Heid, A., De, A., Zhang, W.: Additive manufacturing of metallic components—process, structure and properties. Prog. Mater. Sci. **92**, 112–224 (2018). https://doi.org/10.1016/j.pmatsci.2017.10.001
4. Zhang, X., Yocom, C., Mao, B., Liao, Y.: Microstructure evolution during selective laser melting of metallic materials: a review. J. Laser Appl. **31**, 31201 (2019). https://doi.org/10.2351/1.5085206
5. Zinovieva, O., Zinoviev, A., Romanova, V., Balokhonov, R.: Three-dimensional analysis of grain structure and texture of additively manufactured 316L austenitic stainless steel. Addit. Manuf. **36**, 101521 (2020). https://doi.org/10.1016/j.addma.2020.101521
6. Xiang, D.D., Wang, P., Tan, X., Chandra, S., Wang, C., Nai, M.L.S., Tor, S., Liu, W.Q., Liu, E.: Anisotropic microstructure and mechanical properties of additively manufactured Co–Cr–Mo alloy using selective electron beam melting for orthopedic implants. Mater. Sci. Eng. A **765**, 138270 (2019). https://doi.org/10.1016/j.msea.2019.138270
7. Hitzler, L., Hirsch, J., Tomas, J., Merkel, M., Hall, W., Öchsner, A.: In-plane anisotropy of selective laser-melted stainless steel: the importance of the rotation angle increment and the limitation window. Proc. Inst. Mech. Eng. Part L J. Mater. Des. Appl. **233**, 1419–1428 (2019). https://doi.org/10.1177/1464420718757068
8. Arısoy, Y.M., Criales, L.E., Özel, T., Lane, B., Moylan, S., Donmez, A.: Influence of scan strategy and process parameters on microstructure and its optimization in additively manufactured nickel alloy 625 via laser powder bed fusion. Int. J. Adv. Manuf. Technol. **90**, 1393–1417 (2017). https://doi.org/10.1007/s00170-016-9429-z
9. Ghanavati, R., Naffakh-Moosavy, H.: Additive manufacturing of functionally graded metallic materials: a review of experimental and numerical studies. J. Mater. Res. Technol. **13**, 1628–1664 (2021). https://doi.org/10.1016/j.jmrt.2021.05.022
10. von Kobylinski, J., Lawitzki, R., Hofmann, M., Krempaszky, C., Werner, E.: Micromechanical behaviour of Ni-based superalloys close to the yield point: a comparative study between neutron diffraction on different polycrystalline microstructures and crystal plasticity finite element modelling. Contin. Mech. Thermodyn. **31**, 691–702 (2022). https://doi.org/10.1007/s00161-018-0720-0
11. Robl, T., Krempaszky, C., Fillafer, A., Werner, E.: Examining the unloading behavior of dual-phase steels by means of microstructure simulations. Mater. Sci. Eng. A **823**, 141744 (2021). https://doi.org/10.1016/j.msea.2021.141744
12. Huber, J., Vogler, J., Werner, E.: Multiscale modeling of the mechanical behavior of brazed Ni-based superalloy sheet metals. Contin. Mech. Thermodyn. (2022). https://doi.org/10.1007/s00161-022-01172-x
13. Kouznetsova, V.: Computational Homogenization for the Multi-scale Analysis of Multi-phase Materials. PhD thesis, Mechanical Engineering, Technische Universiteit Eindhoven (2002). https://doi.org/10.6100/IR560009
14. Werner, E., Wesenjak, R., Fillafer, A., Meier, F., Krempaszky, C.: Microstructure-based modelling of multiphase materials and complex structures. Contin. Mech. Thermodyn. **28**, 1325–1346 (2016). https://doi.org/10.1007/s00161-015-0477-7
15. Roters, F.: Advanced material models for the crystal plasticity finite element method: development of a general CPFEM framework. Doctoral dissertation, Publikationsserver der RWTH Aachen University and Aachen, Techn. Hochsch., Habil.-Schr (2011). https://doi.org/10.18154/RWTH-CONV-144865
16. Hitzler, L., Hirsch, J., Heine, B., Merkel, M., Hall, W., Öchsner, A.: On the anisotropic mechanical properties of selective laser-melted stainless steel. Materials **10**, 1136 (2016). https://doi.org/10.3390/ma10101136
17. Vilaro, T., Colin, C., Bartout, J.D.: As-fabricated and heat-treated microstructures of the Ti–6Al–4V alloy processed by selective laser melting. Metall. Mater. Trans. A **42**, 3190–3199 (2011). https://doi.org/10.1007/s11661-011-0731-y
18. El-Tahawy, M., Jenei, P., Kolonits, T., Han, G., Park, H., Choe, H., Gubicza, J.: Different evolutions of the microstructure, texture, and mechanical performance during tension and compression of 316L stainless steel. Metall. Mater. Trans. A **51**, 3447–3460 (2020). https://doi.org/10.1007/s11661-020-05782-5

19. Bachmann, F., Hielscher, R., Schaeben, H.: Texture analysis with MTEX-free and open source software toolbox. Solid State Phenom. **160**, 63–68 (2010). https://doi.org/10.4028/www.scientific.net/SSP.160.63
20. Sun, Z., Tan, X., Tor, S.B., Chua, C.K.: Simultaneously enhanced strength and ductility for 3D-printed stainless steel 316L by selective laser melting. NPG Asia Mater. **10**, 127–136 (2018). https://doi.org/10.1038/s41427-018-0018-5
21. Li, X., Yi, D., Wu, X., Zhang, J., Yang, X., Zhao, Z., Wang, J., Liu, B., Bai, P.: Study on mechanism of structure angle on microstructure and properties of SLM-fabricated 316L stainless steel. Front. Bioeng. Biotechnol. **9**, 778332 (2021). https://doi.org/10.3389/fbioe.2021.778332
22. Marattukalam, J.J., Karlsson, D., Pacheco, V., Beran, P., Wiklund, U., Jansson, U., Hjörvarsson, B., Sahlberg, M.: The effect of laser scanning strategies on texture, mechanical properties, and site-specific grain orientation in selective laser melted 316L SS. Mater. Des. **193**, 108852 (2020). https://doi.org/10.1016/j.matdes.2020.108852
23. Andreau, O., Koutiri, I., Peyre, P., Penot, J.-D., Saintier, N., Pessard, E., de Terris, T., Dupuy, C., Baudin, T.: Texture control of 316L parts by modulation of the melt pool morphology in selective laser melting. J. Mater. Process. Technol. **264**, 21–31 (2019). https://doi.org/10.1016/j.jmatprotec.2018.08.049
24. Casati, R., Lemke, J., Vedani, M.: Microstructure and fracture behavior of 316L austenitic stainless steel produced by selective laser melting. J. Mater. Sci. Technol. **32**(8), 738–744 (2016). https://doi.org/10.1016/j.jmst.2016.06.016
25. Smith, M.: ABAQUS/Standard User's Manual, Version 6.9. Dassault Systèmes Simulia Corp, United States (2009)
26. Fischer, T., Werner, E., Ulankyzy, S., Munz, O.: Crystal plasticity modeling of polycrystalline Ni-base superalloy honeycombs under combined thermo-mechanical loading. Contin. Mech. Thermodyn. **31**, 703–713 (2019). https://doi.org/10.1007/s00161-018-0721-z
27. Rycroft, C.H.: Voro++: A three-dimensional voronoi cell library in C++. Chaos **19**, 041111 (2009). https://doi.org/10.1063/1.3215722
28. Quey, R., Kasemer, M.: The Neper/FEPX project: Free /open-source polycrystal generation, deformation simulation, and post-processing. IOP Conf. Ser. Mater. Sci. Eng. **1249**, 012021 (2022). https://doi.org/10.1088/1757-899x/1249/1/012021
29. Roters, F., Diehl, M., Shanthraj, P., Eisenlohr, P., Reuber, C., Wong, S.L., Maiti, T., Ebrahimi, A., Hochrainer, T., Fabritius, H.-O., Nikolov, S., Friak, M., Fujita, N., Grilli, N., Janssens, K.G.F., Jia, N., Kok, P.J.J., Ma, D., Meier, F., Werner, E., Stricker, M., Weygand, D., Raabe, D.: DAMASK–The Düsseldorf advanced=material simulation kit for modelling multiphysics crystal plasticity, damage, and thermal phenomena from the single crystal up to the component scale. Comput. Mater. Sci. 158, 420–478 (2019). https://doi.org/10.1016/j.commatsci.2018.04.030
30. Gottstein, G.: Physical Foundations of Materials Science. Springer, Berlin (2011). https://doi.org/10.1007/978-3-662-09291-0
31. Fischer, T., Hitzler, L., Werner, E.: Morphological and crystallographic effects in the laser powder-bed fused stainless steel microstructure. Crystals **11**, 672 (2021). https://doi.org/10.3390/cryst11060672
32. Biswas, A., Prasad, M.R.G., Vajragupta, N., ul Hassan, H., Brenne, F., Niendorf, T., Hartmaier, A.: Influence of microstructural features on the strain hardening behavior of additively manufactured metallic components. Adv. Eng. Mater. **21**, 1900275 (2019). https://doi.org/10.1002/adem.201900275
33. Lovett, D.: Tensor Properties of Crystals, 2nd edn. CRC Press, Boca Raton (2018). https://doi.org/10.1201/9780203737286
34. Ledbetter, H.M.: Monocrystal–polycrystal elastic constants of a stainless steel. Phys. Status Solidi (A) **85**, 89–96 (1984). https://doi.org/10.1002/pssa.2210850111
35. Hutchinson, J.W.: Bounds and self-consistent estimates for creep of polycrystalline materials. Proc. R. Soc. of Lond. A **348**, 101–127 (1976). https://doi.org/10.1098/rspa.1976.0027
36. van Nuland, T.F.W., van Dommelen, J.A.W., Geers, M.G.D.: Microstructural modeling of anisotropic plasticity in large scale additively manufactured 316L stainless steel. Mech. Mater. **153**, 103664 (2021). https://doi.org/10.1016/j.mechmat.2020.103664
37. Asaro, R., Needleman, A.: Overview no. 42 texture development and strain hardening in rate dependent polycrystals. Acta Metall. **33**, 923–953 (1985). https://doi.org/10.1016/0001-6160(85)90188-9
38. Li, S., Sitnikova, E.: Representative Volume Elements and Unit Cells: Concepts, Theory and Applications and Implementation. Woodhead Publishing, Sawston (2019). https://doi.org/10.1016/C2017-0-03559-0
39. Boeff, M.: Micromechanical Modelling of Fatigue Crack Initiation and Growth. PhD thesis, Ruhr-Universität Bochum (2016)
40. Fillafer, A., Krempaszky, C., Werner, E.: On strain partitioning and micro-damage behavior of dual-phase steels. Mater. Sci. Eng. A **614**, 180–192 (2014). https://doi.org/10.1016/j.msea.2014.07.029
41. Zhang, H., Diehl, M., Roters, F., Raabe, D.: A virtual laboratory using high resolution crystal plasticity simulations to determine the initial yield surface for sheet metal forming operations. Int. J. Plast. **80**, 111–138 (2016). https://doi.org/10.1016/j.ijplas.2016.01.002
42. Hielscher, R.: Kernel density estimation on the rotation group and its application to crystallographic texture analysis. J. Multivar. Anal. **119**, 119–143 (2013). https://doi.org/10.1016/j.jmva.2013.03.014
43. Schaeben, H., Bachmann, F., Fundenberger, J.-J.: Construction of weighted crystallographic orientations capturing a given orientation density function. J. Mater. Sci. 52, 2077–2090 (2017). https://doi.org/10.1007/s10853-016-0496-1
44. Wang, Y., Yu, C., Xing, L., Li, K., Chen, J., Liu, W., Ma, J., Shen, Z.: A data-driven scheme for quantitative analysis of texture. Metall. Mater. Trans. A **51**, 940–950 (2020). https://doi.org/10.1007/s11661-019-05529-x
45. Biswas, A., Vajragupta, N., Hielscher, R., Hartmaier, A.: Optimized reconstruction of the crystallographic orientation density function based on a reduced set of orientations. J. Appl. Crystallogr. **53**, 178–187 (2020). https://doi.org/10.1107/S1600576719017138
46. Ronneberg, T., Davies, C.M., Hooper, P.A.: Revealing relationships between porosity, microstructure and mechanical properties of laser powder bed fusion 316L stainless steel through heat treatment. Mater. Des. **189**, 108481 (2020). https://doi.org/10.1016/j.matdes.2020.108481
47. Prasad, R.G.M., Biswas, A., Geenen, K., Amin, W., Gao, S., Lian, J., Röttger, A., Vajragupta, N., Hartmaier, A.: Influence of pore characteristics on anisotropic mechanical behavior of laser powder bed fusion-manufactured metal by micromechanical modeling. Adv. Eng. Mater. **22**, 2000641 (2020). https://doi.org/10.1002/adem.202000641

48. Li, C., Liu, J.F., Fang, X.Y., Guo, Y.B.: Efficient predictive model of part distortion and residual stress in selective laser melting. Addit. Manuf. **17**, 157–168 (2017). https://doi.org/10.1016/j.addma.2017.08.014
49. Vrancken, B., Cain, V., Knutsen, R., Van Humbeeck, J.: Residual stress via the contour method in compact tension specimens produced via selective laser melting. Scr. Mater. **87**, 29–32 (2014). https://doi.org/10.1016/j.scriptamat.2014.05.016

Publisher's Note Springer Nature remains neutral with regard to jurisdictional claims in published maps and institutional affiliations.